DNA-Nanostructure–Gold-Nanorod Hybrids for Enhanced In Vivo Optoacoustic Imaging and Photothermal Therapy

Yang Du, Qiao Jiang, Nicolas Beziere, Linlin Song, Qian Zhang, Dong Peng, Chongwei Chi, Xin Yang, Hongbo Guo, Gaël Diot, Vasilis Ntziachristos, Baoquan Ding,* and Jie Tian**

Early diagnosis, accurate staging, and image-guided surgery of tumors remain the major clinical concerns for improving patient survival and treatment outcomes.[1] Currently available conventional imaging techniques are unable to fulfill these demands due to their low sensitivity and specificity, poor spatial resolution, low penetration, and/or harmful ionizing radiation.[2] Molecular imaging research is focused on the imaging and characterization of disease processes effectively at the cellular and molecular level in the living cells, tissues, and intact subjects.[3] Optoacoustic imaging (OAI) is a relatively new molecular imaging technique that brings significant promise to enhance the depth of imaging penetration as well as spatial resolution, and also maintaining the high contrast of optical imaging.[4] OAI has garnered significant interest and is expected to have broad applications in biomedical treatments.[5] Major preclinical applications include imaging of tumors, drug responses, brain and heart function.[2,6] With the use of near-infrared (NIR) laser light, OAI can provide very high penetration depths, even in living tissue, on the order of centimeters.[5] By taking advantage of the individual strengths of optical and acoustic components and by applying a multispectral and tomographic approach termed as multispectral optoacoustic tomography (MSOT), OAI can provide functional and molecular information about abnormalities owing to the deep tissue penetration of the laser light at high sensitivities and at excellent spatial resolutions.[7]

In addition to the rapid development of imaging techniques, there is a pressing need for the engineering of novel probes that can be used in noninvasive combinatory therapeutic–diagnostic applications. Several endogenous proteins such as hemoglobin and melanin function as natural OAI contrast agents and thus allow the evaluation of physiological parameters, while exogenous contrasting agents would undoubtedly benefit this imaging modality by enhancing the image quality and contrast, particularly in cancer research.[7,8] Artificial contrasting agents such as organic dyes and fluorochromes such as the FDA approved cyanine dye indocyanine green (ICG) as well as various light-absorbing nanoparticles such as Au-based nanostructures, carbon nanotubes, and nanodroplets have been developed.[2,9] Although indocyanine green ICG is approved by the FDA and is routinely used in a variety of clinical settings, it suffers from significantly smaller optical absorption cross-section than metal nanoparticles, poor in vivo stability (self-aggregation), poor photostability, and rapid blood clearance rate in the context of OAI.[10] In comparison, the localized surface plasmon resonances (LSPR) provide metal-based particles with strong optoacoustic signal generation and photo-stability, and thereby constitute the "gold standard" for OAI.[11] Recently, gold nanoparticles have attracted significant research interest as nanosized contrast agents in OAI owing to their biocompatibility, unique optical absorption properties, and photothermal (PT) effects.[12]

Photothermal therapy (PT) is a platform to fight cancer due to its high therapeutic efficiency for targeting cells while minimizing the damage to adjacent normal tissues.[13] The particular interest of photothermal therapy is the engineering of multifunctional nanoplatforms to allow the cancer diagnosis and therapy simultaneously.[14] Gold nanoparticles have a great impact on plasmonic photothermal therapy due to their simple synthesis, easy surface functionalization and diverse morphologies.[12,15] Au-based nanostructures have also been approved by FDA as drug carriers or therapeutic agents for various phase I clinical trials.[15c,d] To realize the full potential of gold nanoparticles, an OAI-PT combinatorial approach requires efficient targeting to the diseased tissue. Tailor-made improvements in the basic structure of gold nanorods (AuNRs) using different approaches for the optimization of OAI and PT are currently a major challenge in the field of nanotechnology.

Prof. Y. Du, Dr. Q. Zhang, D. Peng, Dr. C. Chi, Prof. X. Yang, Prof. J. Tian
The Key Laboratory of Molecular Imaging
Chinese Academy of Sciences
The State Key Laboratory of Management and Control for Complex Systems
Institute of Automation
Chinese Academy of Sciences
Beijing 100190, China
E-mail: jie.tian@ia.ac.cn

Dr. Q. Jiang, L. Song, H. Guo, Prof. B. Ding
CAS Key Laboratory of Nanosystem and Hierarchical Fabrication
CAS Center for Excellence in Nanoscience
National Center for Nanoscience and Technology
Beijing 100190, China
E-mail: dingbq@nanoctr.cn

Dr. Q. Jiang
CAS Key Laboratory of Colloid Interface and Chemical Thermodynamics
Institute of Chemistry
Chinese Academy of Sciences
Beijing 100190, China

Dr. N. Beziere, Dr. G. Diot, Prof. V. Ntziachristos
Institute for Biological and Medical Imaging (IBMI)
Helmholtz Zentrum München and Technische Universität München
85764 Neuherberg, Germany
E-mail: v.ntziachristos@tum.de

DOI: 10.1002/adma.201601710

With well-defined nanoscale shapes, uniform sizes, precise spatial addressability, and excellent biocompatibility, DNA-origami nanostructures have been used as template for organization larger nanoparticles such as gold nanoparticles, proteins, and quantum dots to achieve multiple functions.[16] DNA origami has been shown to be a great platform for biomedical applications, facilitating the cellular imaging, targeted payload delivery, and controlled drug release.[13c,17] Our previous work demonstrated that DNA-origami-based nanocarriers can be used for anticancer drug delivery in vivo and displayed enhanced passive tumor-targeting effects and long-acting properties at the tumor region.[18] Compared to other shapes, a triangular-shaped DNA-origami structure exhibited optimum passive tumor targeting and accumulation without observable systemic toxicity.[18] Recent developments in the use of DNA-based nanostructures as tools for cancer diagnosis and therapy have been made based on these superior features.[16b,c,17b,d,18]

Inspired by the above intriguing properties of DNA origami and gold nanorods, here, we demonstrate the construction of a nanoplatform by assembling gold nanorods (AuNRs) on the surface of a DNA-origami structure (D–AuNR) and report the evaluation of its performance in vitro. Subsequently, we also investigated the selectivity and sensitivity of the hybrid nanostructures in tumor detection in vivo by utilizing D–AuNR-enabled multispectral high-resolution OAI. Based on MSOT diagnosis, we utilized the photothermal conversion properties of the D–AuNR to trigger therapeutic activity, monitor activation, and evaluate the photoactivated outcome of the treatment (**Figure 1**). Our study demonstrated that D–AuNRs can function both as an efficient diagnostic tool and as therapeutic agents, thus completing the theranostic package.

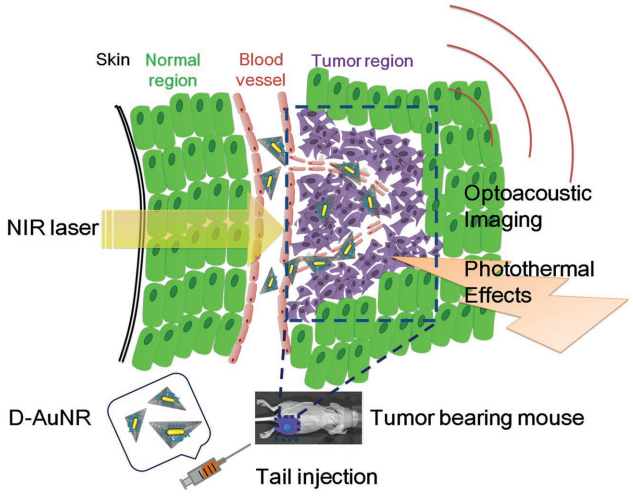

Figure 1. DNA-origami–gold-nanorod hybrid (D–AuNR) nanoprobe system. M13mp18 genomic DNA scaffold strands were self-assembled into triangular-shaped nanostructures with defined binding sites through the hybridization of rationally designed staple and capture strands. Gold nanorods (AuNR) modified by single-strand DNA (complementary to capture strands) were organized at predesignated positions on the surface of the origami through DNA hybridization, thereby generating D–AuNR nanostructures. The D–AuNRs were administered into 4T1-fLuc-xenograft-tumor-bearing mice by tail injection, followed by optoacoustic imaging (OAI) and photothermal therapy.

The D–AuNR nanostructure was synthesized and characterized. A triangular DNA-origami structure was folded based on methods reported by Rothemund[16d] with several modifications. The M13mp18 genomic DNA strand, capture and helper DNA strands were annealed in a ratio of 1:10:10 from 95 °C to room temperature. DNA capture strands with carefully designed sequences were extended from the surface of the origami template to precisely organize one AuNR (42 nm × 12 nm) as shown in Figure S1 and Scheme S1 of the Supporting Information. AuNR functionalized with DNA sequences complementary to the capture strands and purified DNA origami were then mixed and annealed from 45 to 25 °C in 2 h for 30 cycles. After hybridization, AuNRs were assembled at the binding sites on the DNA platform. The raw assembled nanostructures, before and after AuNR loading, were subsequently characterized by agarose gel electrophoresis (AGE) (Figure S1a,b, Supporting Information). Lane 1 and 2 depict the AuNR and raw products of D–AuNR, respectively, which are easily visualized in bright field. Lane 3 corresponds to the bare triangular DNA-origami template, visualized only after ethidium bromide staining under UV illumination. Bands corresponding to target complexes are indicated in boxes. These bands were sliced and extracted from the gel with a freeze–squeeze column (Bio-Rad) at 4 °C, and the purified nanostructures were characterized by transmission electron microscopy (TEM). Images of the plain DNA origami and conjugates of D–AuNR are shown in Figure S1c,d of the Supporting Information. These images provide direct evidence that the formation of D–AuNR and the morphology of the DNA nanostructures were retained after assembly of AuNR.

The AuNRs with localized surface plasmon resonances (LSPR) in the NIR region are ideal agents for two-photon luminescence (TPL) imaging of live cells. After overnight administration of AuNR and D–AuNR to cultured 4T1-fLuc-tumor cells followed by removal of excess nanoparticles and conjugates, live cells were imaged by two-photon-excitation laser-scanning microscopy. As shown in Figure S2a of the Supporting Information, TPL was visible in cells treated with D–AuNR and the bare AuNR, but not in the control group treated with phosphate-buffered saline (PBS), demonstrating successful internalization and accumulation of the D–AuNR and the AuNR in tumor cells. While a signal could be detected in the bare-AuNR-treated tumor cells, its intensity was stronger in tumor cells treated with D–AuNR. Moreover, inductively coupled plasma–mass spectrometry (ICP-MS) can be used to give a precise quantification of the amount of administered gold which has been internalized by cells or tissues.[2,19] Our data showed that there was more gold accumulation in D–AuNR-treated tumor cells than free-AuNR-treated cells (Figure S2b, Supporting Information, $***P < 0.0001$). The above results altogether indicated that the DNA origami functions as an ideal nanocarrier and can efficiently optimize the internalization of AuNR within cancer cells in vitro.

Prior to the in vivo OAI experiments, it is critical to evaluate the sensitivity limit of probes used for OAI in scattering agar phantoms, which emulates the important properties of biological tissues for the purpose of providing a more realistic imaging environment.[20] Specifically, two regions of interest (ROI) in the optoacoustic images of a scattering agar phantom were drawn around inclusions containing the probe and PBS,

ADVANCED MATERIALS
www.advmat.de

www.MaterialsViews.com

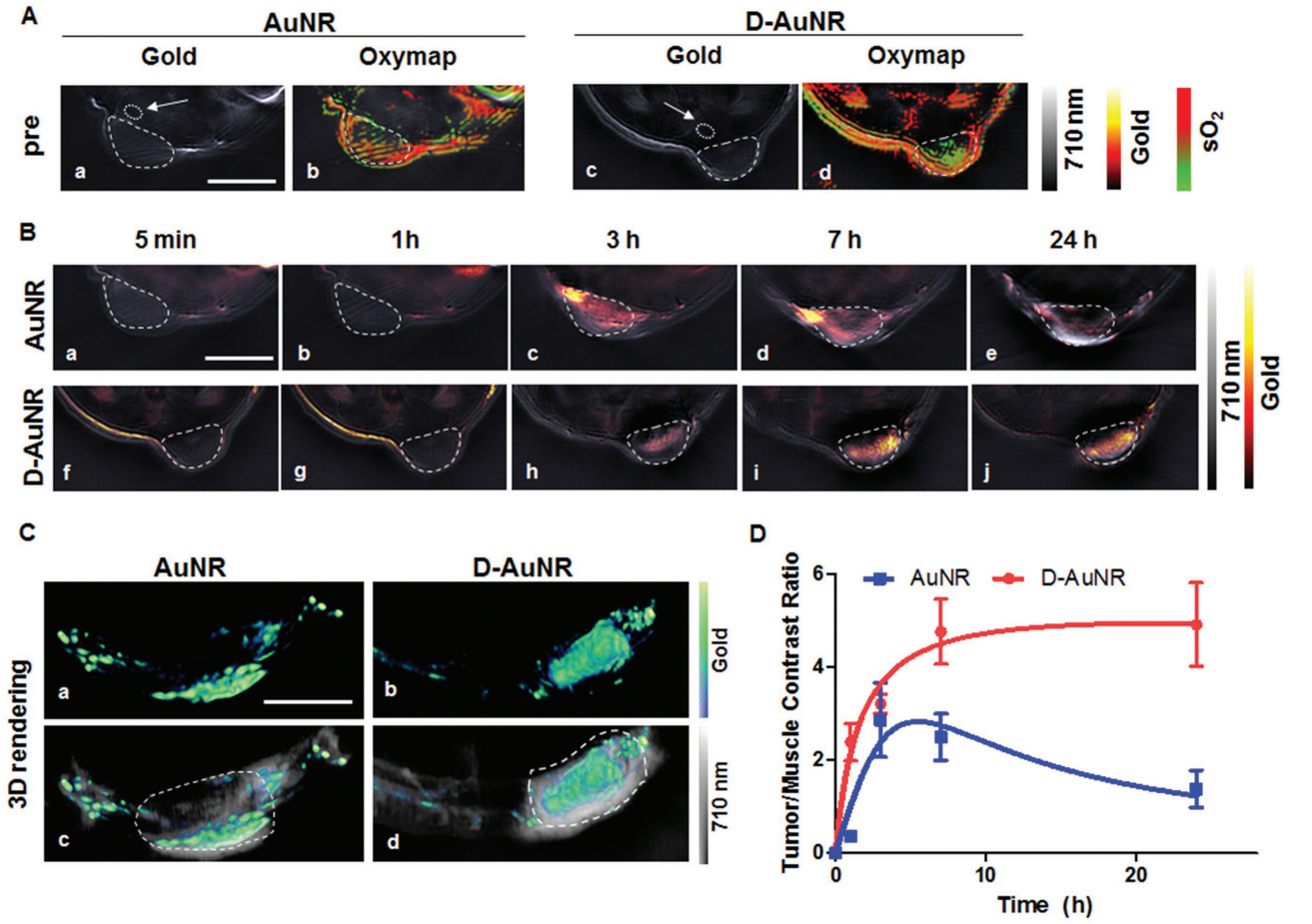

Figure 2. Optoacoustic evaluation of D–AuNR hybrids in vivo. A) The gold distribution (hot scale, a,c) and the corresponding oxygen-saturation maps (green to red scale, b,d) before intravenous injection of AuNR and D–AuNR in 4T1-tumor-bearing mice. B) AuNR and D–AuNR distribution (hot scale) at several time points including 5 min (a,f), 1 h (b,g), 3 h (c,h), 7 h (d,i), 24 h (e,j) after intravenous injection in 4T1-tumor-bearing mice (dashed outlined) overlayed on an optoacoustic image acquired at a single illumination wavelength (710 nm, gray scale). Scale bar = 5 mm. C) 3D rendering the optoacoustic images in the cancerous regions on 4T1-tumor-bearing mice 24 h postinjection of the AuNR (a, hot scale) and D–AuNR (b, hot scale), overlayed on single wavelength images (c,d, 710 nm, gray scale). Scale bar = 5 mm. D) Contrast ratio between the tumor and the region of back muscles extracted from the images for AuNR (blue) and D–AuNR (red). A section of the back muscle (indicated by the white arrows) is outlined in the initial single wavelength image.

following which the signal in the ROIs was measured and averaged amongst the imaging planes. The signal in each inclusion was normalized to the average signal measured for PBS in the dilution range. The lowest limit of quantification was determined as the concentration at which the signal to background ratio remained greater than 1.[21] As shown in Figure S3 of the Supporting Information, both the D–AuNR and the AuNR behaved similarly and displayed a similar signal and a similar slope. For gold containing particles, the detection limit was found to be 78×10^{-12} M. Similar to PBS, the DNA origami alone did not exhibit any absorbance and did not modify the OAI behavior of the AuNR.

OAI was then performed on the breast-tumor-xenografted mice in the tumors, liver, and kidney areas shortly before, and 5 min, 1 h, 3 h, 7 h, and 24 h after intravenous injection of nanoparticles (NPs) in order to investigate the imaging capacity of the engineered D–AuNR compared to classical AuNR in vivo. MSOT signal contributions from AuNR in tumor regions are shown in **Figure 2**. The OAI signals of both AuNR and D–AuNR can be detected in the tumors as early as 3 h postinjection (Figure 2B-c,h). The signal corresponding to D–AuNRs increased gradually from 3 to 7 h postinjection and displayed excellent penetration in the tumor mass (Figure 2B-i), and retention for at least 24 h postinjection (Figure 2B-j). In contrast, although the signal for AuNR was also detected from 3 to 7 h postinjection (Figure 2B-d), its intensity decreased gradually until 24 h postinjection (Figure 2B-e). It is reported that rapid tumor growth results in a drop in the oxygen availability and creates a hypoxic microenvironment.[22] Moreover, the hypoxemia can be visualized through measuring the blood oxygen saturation levels by optoacoustic tomography.[23] In this study, the oxygen saturation (sO_2) maps are calculated and shown in Figure 2A-b,d and Figure S4 of the Supporting Information in the AuNR and D–AuNR tumors, respectively. The result showed that tumors of two groups display a homogeneous albeit hypoxic core, while the surrounding blood vessels mainly show the influx of oxygen-rich hemoglobin. Furthermore, we found that the OAI signal of D–AuNR was mainly distributed

and partially overlapped with the central hypoxic region of tumors, while the signal of AuNR was distributed at the outer parts of tumors. In order to further confirm that, the 3D volume rendering of images (Figure 2C) in the tumor regions on nude mice 24 h postinjection of the AuNR and D–AuNR was performed. The green scale was applied to the nanoparticle signal (AuNR or D–AuNR) and the grey scale to the single wavelength image stacks. Only the tumor and surrounding tissues were reconstructed, omitting the internal organs, in order to increase visibility of the tumor and nanoparticles. The 3D images were produced using a forward 25° tilt along the X axis. The result showed that OAI signal of D–AuNR was mainly distributed in the central region of tumors (Figure 2C-b,d), while the signal of AuNR was distributed at the peripheral parts of tumors (Figure 2C-a,c). Compared to the AuNR, the D–AuNR possessed better tumor accumulation, with an increased retention and deeper penetration of gold within the tumor hypoxic region (Figure 2B-j). Hypoxia and defective vascular architecture are considered as unique pathophysiological characteristics of most solid tumors, which could lead to the enhanced permeability and retention (EPR) effect for macromolecular agents and nanoparticles.[22b,c] Our previous work demonstrated that DNA-origami carriers, particularly triangular-shaped ones, can passively target and accumulate at tumor regions due to EPR effects.[18] Thus, the triangular D–AuNR was used for OAI imaging and further in vivo photothermal therapy.

Moreover, the contrast improvement between AuNR and D–AuNR was also evaluated. Figure 2D shows the contrast ratio, calculated from the regions shown in Figure 2A-a,c, between the back muscles and the tumor regions after injection of AuNR and D–AuNR. In comparison to AuNR, where the contrast ratio culminated around 3 and dropped steadily after 3 h, the contrast ratio in D–AuNR remained around 5. Extraction of the average gold signal values in these two organs emphasizes the enhancement of a high and stable contrast provided by D–AuNR as an OAI diagnosis tool. While a minor amount of gold particles was detected in the liver, almost no signal was observed in the kidney region in both instances (Figure S5, Supporting Information). The results altogether suggested that DNA-origami nanocarriers could facilitate the accumulation of AuNRs into the core areas of tumors in vivo, thereby enhancing the OAI signals at these regions.

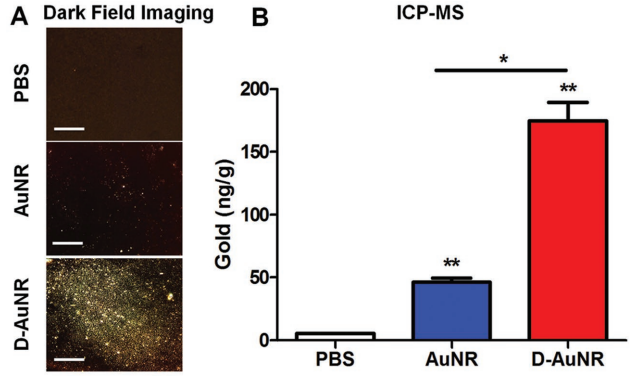

Figure 3. Dark-field imaging and ICP-MS of D–AuNR in tumor tissues. A) Dark-field images of control, AuNR, and D–AuNR. Scale bar = 20 µm. B) Detection of gold signals by ICP-MS and comparison in tumor tissues from different treatment groups (*$P < 0.05$, **$P < 0.01$). A higher detection of gold content in the D–AuNR-treated tumor tissues suggested that it could facilitate the in vivo observation and detection of tumors.

To further confirm the in vivo OAI observation, we performed the dark-field imaging and ICP-MS of D–AuNR in tumors and major organ tissues. The dark-field imaging data showed that no signal was observed in the blank group, whereas a weak signal was detected in the AuNR-treated tumor tissues (**Figure 3**A). Stronger signals were observed in the D–AuNR-treated tumor tissues compared to the other two groups. Our ICP-MS of tumor tissues data also revealed a similar result with dark-field imaging of frozen tumor sections (Figure 3B). The ICP-MS results showed that the gold signals in tumor tissues treated with D–AuNR were significantly higher than tissues treated with AuNR (*$P < 0.05$). Additionally, dark-field imaging indicated that gold signals were highly reduced in the liver and kidney tissues in case of the D–AuNR-treated groups compared to the AuNR-treated groups (Figure S6, Supporting Information). Thus, results of dark-field imaging and ICP-MS were consistent with the in vivo OAI observation and the facilitative role of the D–AuNR for in vivo observation and detection of tumors was confirmed. The enhancement in AuNR OAI signals was a result of its increased accumulation at tumor site through DNA-origami nanocarriers confirmed by the dark-field imaging and ICP-MS analyses (Figure 3). Taken together, our results proved the enhanced tumor-targeting properties and stable OAI signal detection following the systemic administration of D–AuNRs in vivo. More importantly, this study suggested the function of the D–AuNR nanoplatforms as an appropriate and sensitive probe for MSOT imaging, enabling high resolution detection of signals from tumor tissues in live animals.

In addition, the NIR-responsive photothermal therapeutic efficacy of D–AuNR was also tested in this study. For this purpose, the in vitro therapeutic effects of different nanoparticle (NP) formulations after NIR irradiation on 4T1-fLuc tumor cells were compared, and cell viability was assayed by using a cell-counting kit. As shown in **Figure 4**A, the DNA origami alone, similar to the PBS treatment in the control group, did not affect the cell viability and amounted to 95.34% relative to the PBS treatment. Treatment with bare AuNR in addition to laser irradiation led to a significant decrease in cell survival, and cell viability reduced to ≈63% relative to that in the control. Compared to treatment with AuNR alone, D–AuNR treatment combined with laser irradiation led to dramatic suppression of cell viability, which reduced to ≈12.26%. This suggested an enhanced photothermal therapeutic efficacy in tumor cells upon D–AuNR treatment. A possible underlying reason is the increased AuNR internalization by tumor cells after their loading on DNA-origami nanocarriers as demonstrated in Figure S2 of the Supporting Information.

The robustness and reproducible photothermal features of our D–AuNR hybrids structures were demonstrated by investigating the capacity of different groups to respond to NIR stimuli and their photothermal conversion capability in vivo. Mice bearing 4T1-fLuc tumors were intravenously injected with different treatments (PBS, AuNR, and D–AuNR) and irradiated with NIR laser, and the results were shown in Figure 4B. NIR irradiation in the PBS group led to a slight

ADVANCED MATERIALS
www.advmat.de

Materials Views
www.MaterialsViews.com

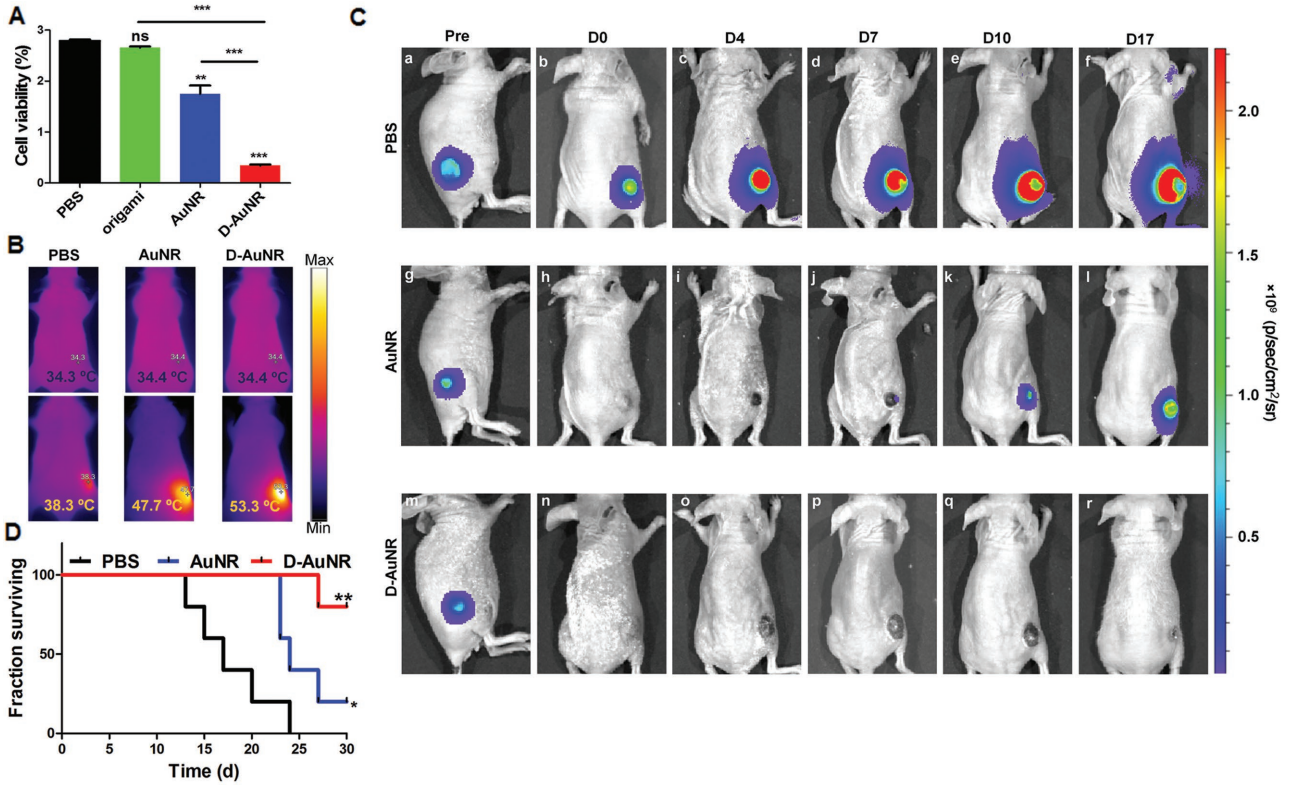

Figure 4. Efficiency of photothermal therapy using plain AuNR and D–AuNR. A) Cell viability of 4T1-fLuc tumor cells after administration with PBS, DNA origami, AuNR, D–AuNR, and NIR laser irradiation (808 nm, 1.5 W cm^{-2}, 3 min) (**P < 0.01, ***P < 0.0001). B) Infrared thermographic maps of mice subjected to intravenous administration of PBS, AuNR, and D–AuNR measured 10 min after NIR irradiation (808 nm, 1.5 W cm^{-2}). C) Bioluminescence imaging (BLI) of 4T1-fLuc-tumor-bearing mice intravenously injected with PBS in the control group, AuNR and D–AuNR (10×10^{-9} M, 150 µL), followed by 10 min NIR laser irradiation. Images were taken at Pre, day 0, 4, 7, 10, and 17 d (Pre, D0, D4, D7, D10, and D17) respectively. D) Survival rates of mice bearing 4T1-fLuc tumors after photothermal therapy. The survival rates of mice were monitored for 30 d postinjection. The blue, green, and red lines represent the survival rates of the Control, AuNR, and D–AuNR groups, respectively. (*P < 0.05, **P < 0.01).

elevation in temperature from 34.3 to 38.3 °C, while administration of AuNR followed by NIR irradiation resulted in a temperature rise up to 47.7 °C. D–AuNR treatment combined with irradiation induced the highest temperature increase with a local temperature maximum of 53.3 °C. These results suggested that the D–AuNR leads to elevation of local temperatures during in vivo photothermal therapy, which may enhance the outcome of tumor therapy.

To validate the above hypothesis, we furtherly used bioluminescence imaging (BLI) to investigate the photothermal therapeutic effects of D–AuNR in 4T1-fLuc-tumor-bearing nude mice (Figure 4C). BLI permits rapid, sensitive and noninvasive in vivo detection and quantification of tumor cells specifically engineered to emit visible light. It offers quantitative and sensitive analysis of tumor growth, regression, and metastasis on traditional oncology animal models.[24] The survival time of every mouse in the different treatment groups was recorded after photothermal therapy (Figure 4D). Tumors grew rapidly after treatment with PBS control and laser irradiation, resulting in a high mortality rate in this group (within 30 d after treatment); this suggested that laser irradiation alone was incapable of impairing tumor growth (Figure 4C-a–f). Tumors subjected to treatment with AuNRs combined with laser irradiation suffered burns, which turned into a black scar on the tumor surface. A minor BLI signal, presumably arising from remaining 4T1-fLuc tumor cells, was detected at the tumor site few days after the treatment. However, recurrence of the tumor was not observed upon visual inspection (Figure 4C-h,i). The BLI signal intensity increased gradually (Figure 4C-j–l) and was accompanied by the recurrence of tumors surrounding the scar. The survival rate dropped to 20% on post-treatment day 30 (*P < 0.05). Complete remission of tumors was achieved after laser irradiation in mice treated with D–AuNR, resulting in black scars at the original site accompanied by an undetectable level of BLI signals during the 17 d observation period (Figure 4C-n–r). No tumor reformation was observed. The survival rate of mice was 80% on post-treatment day 30 (**P < 0.01). The BLI intensity was further analysed, and the data were consistent with our observation (Figure S7, Supporting Information). These results demonstrated the photothermal therapeutic efficiency of D–AuNR along with an improved inhibitory effect of tumor recurrence in comparison to the bare AuNR. The body weight was also measured before and after photothermal therapy for safety assessment. Compared to the PBS-treated group, the body weight of tumor-bearing mice in the AuNR and D–AuNR groups did not decrease during the 17 d observation (Figure S8, Supporting Information). All these results exhibited that D–AuNRs served as an OAI-guided, NIR-responsive photothermal therapeutic

platform. Both the in vitro and in vivo experiments demonstrated the selectivity of this platform in AuNR delivery to target cancer cells, and effective tumor suppression upon NIR irradiation through photothermal therapy. Previous work pointed out that intratumoral administration of self-assembling DNA nanostructures could inhibit tumor growth, which constituted an initial step toward testing the efficacy of the NIR-responsive photothermal therapeutic platform. However, systemic delivery of drugs is usually considered a more realistic strategy in clinical practice.[25] In this context, our results demonstrate effective tumor inhibition through improved systemic intravenous administration of D–AuNRs in the 4T1-tumor-bearing mouse model. The D–AuNR platform incorporates DNA-origami nanostructures due to which AuNR loading can be precisely controlled for optimal biodistribution and accumulation for further systemic administration. A higher local concentration of D–AuNRs than that of AuNRs after administration of identical amount of particles and exposure to the identical light energy resulted in a significant increase in the attainable temperature in the diseased tissue (53.3 vs 47.7 °C). This led to an improved therapeutic outcome of the treatment where the survival rate 30 d after irradiation was significantly improved.

In summary, we have developed an optoacoustic imaging agent by self-assembling gold nanorods onto DNA-origami nanostructures. The gold-nanorod–DNA-nanostructure hybrid, which combines the advantages of gold nanorods with those of the DNA-origami structure, serves as a unique probe and an efficient contrast agent in OAI and allows improved imaging quality and decreased dose. Simultaneously, D–AuNRs responded to NIR irradiation for the photothermal therapy and effectively inhibited tumor regrowth and prolonged the survival of diseased mice. We believe that this system could be successfully incorporated in different disease-specific targeting ligands and imaging components for an improved OAI efficiency and treatment efficacy. Since the OAI modality utilizes nonionizing radiation and is therefore safe for patients and medical staff, we expect that the combination of OAI with the theranostic agent developed here will encourage further studies investigating its potential in clinical translation in the near future.

Experimental Section

Materials and Reagents: Oligonucleotides (origami staple strands, capture strands, and 3′thiol-modified strands) were purchased from Invitrogen (Shanghai, China). The origami staple strands and capture strands were stored in 1.5 mL Eppendorf tubes after normalizing concentrations to 100×10^{-3} M and were used without further purification. All 3′thiol-modified DNA strands were purified by denaturing polyacrylamide gel electrophoresis (PAGE). Concentration of each strand was estimated by measuring its UV absorbance at 260 nm. M13mp18 phage single-stranded DNA was purchased from New England Biolabs, Inc. (N4040S, Beijing, China). Sodium borohydride ($NaBH_4$), auric acid ($HAuCl_4$), cetyltrimethylammonium bromide (CTAB), silver nitrate ($AgNO_3$), and tris (carboxyethyl) phosphine hydrochloride (TCEP) were purchased from Sigma–Aldrich.

Synthesis of Triangular D–AuNR: i) Synthesis of AuNRs: Seed-mediated growth was performed to synthesize gold nanorods according to the method of Nikoobakht and El-Sayed.[26] ii) Modification of AuNRs with thiolated DNA: AuNRs were modified with oligo-DNA at low pH value according to the method of Ding and co-workers.[27] ii) DNA-origami assembly and purification: Triangular DNA-origami structures were self-assembled according to the methods described by Rothemund.[16d] The M13mp18 ssDNA (5×10^{-9} M), short staple strands, and capture strands (unpurified) were used at a molar ratio of 1:10:10. The DNA origami was annealed and assembled in TAE-Mg^{2+} buffer (Tris, 40×10^{-3} M; acetic acid, 20×10^{-3} M; EDTA, 2×10^{-3} M; magnesium acetate, 12.5×10^{-3} M; pH 8.0) in a thermocycler (Eppendorf China) by slow cooling from 90 °C to room temperature over 12 h. DNA origami with capture strands was then filtered using 100 kDa MWCO centrifuge filters (Amicon, Millipore) to remove extra staple and capture strands. iv) Self-assembly of AuNR–origami conjugates: Purified DNA origami was mixed with oligo-DNA modified AuNR at a ratio of 2:1 for AuNR to the binding site on the surface of DNA origami. This mixture was annealed from 45 to 25 °C in 2 h for 30 cycles.

Cell Culture: 4T1-fLuc mouse breast-cancer cells were cultured in 1640 Medium (Life Technologies, USA) and supplemented with 10% fetal calf serum (FCS) (Life Technologies, USA). Cells were maintained at 37 °C in 5% CO_2.

Establishment of a Breast Tumor Xenograft Mouse Model: All animal experiments were performed according to the guidelines of the Institutional Animal Care and Use Committee of Peking University (Permit Number: 2011-0039), and the District Government of Upper Bavaria (Az.: 55.2.1-54-2532-102-11). Briefly, five-week old athymic female BALB/c nude mice were purchased from the Department of Experimental Animals, Peking University Health Science Center. Tumors were initiated by injecting 1×10^6 4T1-fLuc cells subcutaneously (s.c.) in the back of the BALB/c nude mice. Mice displaying tumor volumes around 100 mm^3 were randomly divided into three groups (4 mice per group): control, AuNR, and D–AuNR groups.

Optoacoustic Imaging of Probes In Vitro: OAI was performed on both the scattering agar phantom and the in vivo tumor mouse model by using MSOT inVision 256 small animal scanner, and the acquisition data were processed using the ViewMSOT software (iThera Medical GmbH, Munich, Germany), unless stated otherwise. It has been demonstrated the improved resolution and overall image quality for the increased number of detectors used pointing to significant improvements in image quality for the 256 detector array, over 64 or 128 detectors.[28] The OAI signals of AuNR and D–AuNR in the scattering agar phantom were tested. The phantom was made according to the previous work as following: briefly, cylindrical phantom with 2 cm diameter was prepared by using a gel made from distilled water containing Agar (1.3% w/w) (Sigma–Aldrich, USA) and intralipid 20% emulsion (6% v/v) (Sigma–Aldrich, USA), resulting in a gel with a reduced scattering coefficient of $m's \approx 10\ cm^{-1}$.[9b,29] Aqueous solutions of each formulation were placed into a 2 mm diameter plastic inclusion in the scattering agar phantom along with a PBS inclusion as a control to determine the optoacoustic spectra. For each probe dilution, five individual measurements was performed at different positions of the phantom at a distance of 2 mm one from the other. Thus, the mean and SD are based on these five measurements. Following a tomographic model-matrix inversion reconstruction of the data,[30] a linear spectral unmixing was carried out.

Optoacoustic Imaging of Probes In Vivo: Furthermore, OAI of the tumor, liver, and kidney areas was performed on the 4T1 tumor xenograft mouse model by using the same MSOT system and processing software. OA signal was recorded at different time points before and after intravenous injection of AuNR (7×10^{-9} M, 150 µL) or D–AuNR (7×10^{-9} M, 150 µL) to examine their biodistribution. Time points included one recording before injection (pre) and at 5 min, 1 h, 3 h, 7 h, and 24 h after injection. Data were reconstructed using a model-based approach. Unmixing was performed using the least square method using hemoglobin, oxygenated hemoglobin, and the absorbance spectra of the compound used for the experiment to provide the distribution maps of those three photoabsorbers.[30] The oxygen saturation (sO_2) was calculated using the hemoglobin (Hb) and oxygenated hemoglobin (HbO_2) distribution maps obtained previously, by using the following formula in MatLab (Equation (1)):

$$sO_2 = \frac{[HbO_2]}{[Hb]+[HbO_2]} \quad (1)$$

The sO_2 maps are represented as transparent overlays, using 5% of the maximum [Hb] + [HbO_2] as a representation threshold.

For the evaluation of contrast improvement, two distinct regions of interest, namely, the back muscle, located along the spine ("muscle") and the entire tumor ("tumor") were selected and are represented. The average signal in these ROIs from spectrally unmixed gold nanoparticles was extracted, and the ratio between the tumor signal and the muscle signal presented as a function of time. Regions were selected to encompass the entirety of the tumor mass, excluding the surrounding tissue and blood vessels for the tumor, and a section of the back muscle (indicated by the white arrows) alongside the spleen for the muscle.

3D rendering of the distribution of the nanoparticles in the tumors was performed using Amira (Zuse Institute, Berlin, Germany). Briefly, 2D image stacks from the optoacoustic imaging experiments were imported and rendered using the VRT Volren module. Adding a 25% transparency to the gray scale was applied to the single wavelength image stacks, and no transparency to the green scale for the molecular images of the nanoparticles. Only the tumor and surrounding tissues were reconstructed, omitting the internal organs, in order to increase visibility of the tumor and nanoparticles. The images of the rendering were taken using a forward 25° tilt along the X axis.

Dark-Field Imaging: Mice were euthanized 24 h after intravenous injection of AuNR (7×10^{-9} M, 150 µL) or D–AuNR (7×10^{-9} M, 150 µL). Tumors as well as other major organs including the liver, spleen, and kidney were collected for microscopic analysis performed by cryosectioning (CM 1950, Leica Microsystems, Wetzlar, Germany), and observation under Zeiss Imager. A2 microscope mounted with a darkfield condenser (NA = 0.6–0.9) and 20× objective. Pictures were recorded by a piA2400-17 gm gc^{-1} color camera (Basler, Germany).

ICP-MS Sample Preparation and Detection: Mice were euthanized 24 h after intravenous injection of AuNR (7×10^{-9} M, 150 µL) or D–AuNR (7×10^{-9} M, 150 µL), and the tumor tissues were collected. All the samples were completely digested in acid (3:1 mixture of HNO_3 and H_2O_2) on a hot plate prior to ICP analysis. The detection of gold contents in samples treated with AuNR or D–AuNR was performed by mass spectrometry (NexIon 300X, PerkinElmer).

Photothermal Therapy: For in vitro photothermal therapy, the 4T1-fLuc cells were plated in 96-well plates and incubated overnight with control, AuNR (3×10^{-9} M) or D–AuNR (3×10^{-9} M). Cells were irradiated on the following day with near infrared (NIR) laser (808 nm, 1.5 W cm^{-2}) for 3 min. Cell viability was assayed by a cell-counting kit (cck-8, Dojindo, Japan).

For in vivo photothermal therapy, the 4T1-fLuc-tumor-xenograft-bearing mice were randomly divided into three groups (5 mice per group), and were intravenously injected with control PBS, AuNR (10×10^{-9} M, 150 µL) or D–AuNR (10×10^{-9} M, 150 µL). NIR irradiation (808 nm, 1.5 W cm^{-2}) was performed on the tumor xenografts for 10 min at 24 h after injection. Laser irradiation was performed under 2% isoflurane anesthesia, and all efforts were made to minimize suffering. Moreover, after treatment, the mice were monitored for the body weight, food intake, mobility etc., and we did not find the signs of abnormalities.

In Vivo BLI of Tumor Xenografts: For the evaluation of photothermal therapeutic effects in vivo, BLI was dynamically implemented on the breast tumor xenograft mouse model after photothermal therapy by using an IVIS Imaging Spectrum System (PerkinElmer, USA). Ten minutes prior to initiation of BLI, the mice, kept in the prone position, received an intraperitoneal injection of D-luciferin solution (40 mg mL^{-1}, 80 µL) under 2% isoflurane anesthesia. Parameters for the BLI imaging system were set to binning = 4 and exposure time = 1 s. The BLI light intensity was measured by IVIS Living Image 3.0 software (PerkinElmer, USA). The region of interest of the tumor on each mouse was quantitatively analyzed through bioluminescence light intensity. Bioluminescence images were normalized and reported as photons per centimeter square per second (p cm^{-2} s^{-1}). The BLI was taken at different time points including Pre (the day before therapy), day 0 (the day right after therapy), and day 4, 7, 10, and 17.

Survival Rate of Tumor-Bearing Mice after Photothermal Therapy: The tumor-xenograft-bearing mice were kept alive after photothermal therapy, and death of mice from each group was recorded for 30 d for calculation of the survival rate.

Statistics: Data are presented as an average of three independent experiments. One-way analysis of variance (ANOVA) and Tukey's multiple comparisons test or Student's *t*-test was used to determine significant differences. *indicates *P*-values of <0.05, and **indicates *P*-values of <0.01, and both were considered to be statistically significant. Statistical analysis was conducted using Prism 4.0 (San Diego, CA, USA). Survival rate was tested using the Kaplan–Meier method and evaluated with the log-rank test with Bonferroni correction. Differences with *P*-value less than 0.05 were considered statistically significant.

Supporting Information

Supporting Information is available from the Wiley Online Library or from the author.

Acknowledgements

Y.D., Q.J., and N.B. contributed equally to this work. The authors would like to thank Dr. Thomas Sardella from iThera Medical GmbH, Munich, Germany and Dr. Rui Wang from Cold Spring Biotech Corp, Beijing, China for their technical support with phantom MSOT experiments. This work was supported by the National Natural Science Foundation of China (81227901, 81470083, 61231004, 21573051, and 81501594), the Research and Development Program of China (973) under Grant Nos. 2014CB748600, 2015CB755500, and 2012CB934000, Beijing Natural Science Foundation (L140008), Beijing Municipal Science & Technology Commission (Nos. Z161100000116036, Z151100001615012), CAS Interdisciplinary Innovation Team, the Cluster of Excellence "Nanosystem Initiative Munich", the Deutsche Forschungsgemeinschaft (DFG), Sonderforschungsbereich-824 (SFB-824), subproject A1 and the ERC Advanced Grant (233161) "Next Generation in vivo imaging platform for post-genome biology and medicine MSOT". This work was supported in part by the Instrument Developing Project of the Chinese Academy of Sciences under Grant No. YZ201359.

Received: March 30, 2016
Revised: August 16, 2016
Published online: September 28, 2016

[1] a) T. F. Massoud, S. S. Gambhir, *Gene Dev.* **2003**, *17*, 545; b) E. L. Kaijzel, G. van der Pluijm, C. W. G. M. Lowik, *Clin. Cancer Res.* **2007**, *13*, 3490.
[2] C. Kim, E. C. Cho, J. Y. Chen, K. H. Song, L. Au, C. Favazza, Q. A. Zhang, C. M. Cobley, F. Gao, Y. N. Xia, L. H. V. Wang, *ACS Nano* **2010**, *4*, 4559.
[3] a) R. Weissleder, *Science* **2006**, *312*, 1168; b) J. K. Willmann, N. van Bruggen, L. M. Dinkelborg, S. S. Gambhir, *Nat. Rev. Drug Discovery* **2008**, *7*, 591; c) M. L. James, S. S. Gambhir, *Physiol. Rev.* **2012**, *92*, 897; d) M. Ferrari, *Nat. Rev. Cancer* **2005**, *5*, 161.
[4] L. V. Wang, *Nat. Photonics* **2009**, *3*, 503.
[5] V. Ntziachristos, *Nat. Methods* **2010**, *7*, 603.
[6] a) A. Taruttis, V. Ntziachristos, *Nat. Photonics* **2015**, *9*, 219; b) A. Taruttis, G. M. van Dam, V. Ntziachristos, *Cancer Res.* **2015**, *75*, 1548; c) K. Jansen, A. F. W. van der Steen, H. M. M. van Beusekom, J. W. Oosterhuis, G. van Soest, *Opt. Lett.* **2011**, *36*, 597; d) X. D. Wang, Y. J. Pang, G. Ku, X. Y. Xie, G. Stoica, L. H. V. Wang,

Nat. Biotechnol. **2003**, *21*, 803; e) B. Wang, E. Yantsen, T. Larson, A. B. Karpiouk, S. Sethuraman, J. L. Su, K. Sokolov, S. Y. Emelianov, *Nano Lett.* **2009**, *9*, 2212; f) E. Herzog, A. Taruttis, N. Beziere, A. A. Lutich, D. Razansky, V. Ntziachristos, *Radiology* **2012**, *263*, 461; g) T. N. Erpelding, C. Kim, M. Pramanik, L. Jankovic, K. Maslov, Z. J. Guo, J. A. Margenthaler, M. D. Pashley, L. H. V. Wang, *Radiology* **2010**, *256*, 102.

[7] V. Ntziachristos, D. Razansky, *Chem. Rev.* **2010**, *110*, 2783.

[8] a) J. R. Rajian, P. L. Carson, X. D. Wang, *Opt. Express* **2009**, *17*, 4879; b) X. M. Yang, S. E. Skrabalak, Z. Y. Li, Y. N. Xia, L. H. V. Wang, *Nano Lett.* **2007**, *7*, 3798.

[9] a) C. C. Bao, N. Beziere, P. del Pino, B. Pelaz, G. Estrada, F. R. Tian, V. Ntziachristos, J. M. de la Fuente, D. X. Cui, *Small* **2013**, *9*, 68; b) N. Beziere, N. Lozano, A. Nunes, J. Salichs, D. Queiros, K. Kostarelos, V. Ntziachristos, *Biomaterials* **2015**, *37*, 415; c) E. I. Galanzha, E. V. Shashkov, T. Kelly, J. W. Kim, L. L. Yang, V. P. Zharov, *Nat. Nanotechnol.* **2009**, *4*, 855; d) Y. D. Jin, C. X. Jia, S. W. Huang, M. O'Donnell, X. H. Gao, *Nat. Commun.* **2010**, *1*, 41; e) L. S. Bouchard, M. S. Anwar, G. L. Liu, B. Hann, Z. H. Xie, J. W. Gray, X. D. Wang, A. Pines, F. F. Chen, *Proc. Natl. Acad. Sci. USA* **2009**, *106*, 4085; f) A. de la Zerda, Z. A. Liu, S. Bodapati, R. Teed, S. Vaithilingam, B. T. Khuri-Yakub, X. Y. Chen, H. J. Dai, S. S. Gambhir, *Nano Lett.* **2010**, *10*, 2168.

[10] T. Ishizawa, N. Fukushima, J. Shibahara, K. Masuda, S. Tamura, T. Aoki, K. Hasegawa, Y. Beck, M. Fukayama, N. Kokudo, *Cancer* **2009**, *115*, 2491.

[11] S. Mallidi, T. Larson, J. Tam, P. P. Joshi, A. Karpiouk, K. Sokolov, S. Emelianov, *Nano Lett.* **2009**, *9*, 2825.

[12] F. Jabeen, M. Najam-ul-Haq, R. Javeed, C. W. Huck, G. K. Bonn, *Molecules* **2014**, *19*, 20580.

[13] a) L. Cheng, C. Wang, L. Z. Feng, K. Yang, Z. Liu, *Chem. Rev.* **2014**, *114*, 10869; b) G. S. Hong, S. O. Diao, A. L. Antaris, H. J. Dai, *Chem. Rev.* **2015**, *115*, 10816; c) H. S. Jung, J. Han, J. H. Lee, J. H. Lee, J. M. Choi, H. S. Kweon, J. H. Han, J. H. Kim, K. M. Byun, J. H. Jung, C. Kang, J. S. Kim, *J. Am. Chem. Soc.* **2015**, *137*, 3017.

[14] a) J. C. Ge, Q. Y. Jia, W. M. Liu, L. Guo, Q. Y. Liu, M. H. Lan, H. Y. Zhang, X. M. Meng, P. F. Wang, *Adv. Mater.* **2015**, *27*, 4169; b) Y. Park, H. M. Kim, J. H. Kim, K. C. Moon, B. Yoo, K. T. Lee, N. Lee, Y. Choi, W. Park, D. Ling, K. Na, W. K. Moon, S. H. Choi, H. S. Park, S. Y. Yoon, Y. D. Suh, S. H. Lee, T. Hyeon, *Adv. Mater.* **2012**, *24*, 5755.

[15] a) X. H. Huang, P. K. Jain, I. H. El-Sayed, M. A. El-Sayed, *Laser Med. Sci.* **2008**, *23*, 217; b) E. B. Dickerson, E. C. Dreaden, X. H. Huang, I. H. El-Sayed, H. H. Chu, S. Pushpanketh, J. F. McDonald, M. A. El-Sayed, *Cancer Lett.* **2008**, *269*, 57; c) Aurimune (CYT-6091) is a colloidal gold-based tumor-targeted nanomedicine platform. In Phase I clinial trial, CYT-6091 carries TNF into tumors safely and highly effective, http://www.cytimmune.com, accessed: December 2015; d) Aurimune (CYT-6091) is a colloidal gold-based tumor-targeted nanomedicine platform. In Phase I clinial trial, CYT-6091 carries TNF into tumors safely and highly effective, http://www.nanospectra.com, accessed: December 2015.

[16] a) X. W. Liu, Y. Xu, T. Yu, C. Clifford, Y. Liu, H. Yan, Y. Chang, *Nano Lett.* **2012**, *12*, 4254; b) S. M. Douglas, I. Bachelet, G. M. Church, *Science* **2012**, *335*, 831; c) V. J. Schuller, S. Heidegger, N. Sandholzer, P. C. Nickels, N. A. Suhartha, S. Endres, C. Bourquin, T. Liedl, *ACS Nano* **2011**, *5*, 9696; d) P. W. K. Rothemund, *Nature* **2006**, *440*, 297.

[17] a) J. Li, C. H. Fan, H. Pei, J. Y. Shi, Q. Huang, *Adv. Mater.* **2013**, *25*, 4386; b) P. F. Zhan, Q. Jiang, Z. G. Wang, N. Li, H. Y. Yu, B. Q. Ding, *ChemMedChem* **2014**, *9*, 2013; c) J. Li, H. Pei, B. Zhu, L. Liang, M. Wei, Y. He, N. Chen, D. Li, Q. Huang, C. H. Fan, *ACS Nano* **2011**, *5*, 8783; d) Q. Jiang, C. Song, J. Nangreave, X. W. Liu, L. Lin, D. L. Qiu, Z. G. Wang, G. Z. Zou, X. J. Liang, H. Yan, B. Q. Ding, *J. Am. Chem. Soc.* **2012**, *134*, 13396.

[18] Q. Zhang, Q. Jiang, N. Li, L. R. Dai, Q. Liu, L. L. Song, J. Y. Wang, Y. Q. Li, J. Tian, B. Q. Ding, Y. Du, *ACS Nano* **2014**, *8*, 6633.

[19] A. M. Alkilany, P. K. Nagaria, C. R. Hexel, T. J. Shaw, C. J. Murphy, M. D. Wyatt, *Small* **2009**, *5*, 701.

[20] a) J. R. Cook, R. R. Bouchard, S. Y. Emelianov, *Biomed. Opt. Express* **2011**, *2*, 3193; b) P. Di Ninni, F. Martelli, G. Zaccanti, *Phys. Med. Biol.* **2011**, *56*, N21; c) T. Durduran, R. Choe, J. P. Culver, L. Zubkov, M. J. Holboke, J. Giammarco, B. Chance, A. G. Yodh, *Phys. Med. Biol.* **2002**, *47*, 2847.

[21] A. de la Zerda, S. Bodapati, R. Teed, M. L. Schipper, S. Keren, B. R. Smith, J. S. T. Ng, S. S. Gambhir, *Mol. Imaging Biol.* **2010**, *12*, 500.

[22] a) M. C. Brahimi-Horn, J. Chiche, J. Pouyssegur, *J. Mol. Med.* **2007**, *85*, 1301; b) H. Maeda, J. Wu, T. Sawa, Y. Matsumura, K. Hori, *J. Controlled Release* **2000**, *65*, 271; c) V. Torchilin, *Adv. Drug Delivery Rev.* **2011**, *63*, 131.

[23] X. D. Wang, X. Y. Xie, G. N. Ku, L. H. V. Wang, G. Stoica, *J. Biomed. Opt.* **2006**, *11*, 024015.

[24] D. E. Jenkins, Y. Oei, Y. S. Hornig, S. F. Yu, J. Dusich, T. Purchio, P. R. Contag, *Clin. Exp. Metastasis* **2003**, *20*, 733.

[25] a) Z. Y. Xiao, C. W. Ji, J. J. Shi, E. M. Pridgen, J. Frieder, J. Wu, O. C. Farokhzad, *Angew. Chem., Int. Ed.* **2012**, *51*, 11853; b) M. B. Zheng, C. X. Yue, Y. F. Ma, P. Gong, P. F. Zhao, C. F. Zheng, Z. H. Sheng, P. F. Zhang, Z. H. Wang, L. T. Cai, *ACS Nano* **2013**, *7*, 2056.

[26] B. Nikoobakht, M. A. El-Sayed, *Chem. Mater.* **2003**, *15*, 1957.

[27] D. W. Shi, C. Song, Q. Jiang, Z. G. Wang, B. Q. Ding, *Chem. Commun.* **2013**, *49*, 2533.

[28] A. Dima, N. C. Burton, V. Ntziachristos, *J. Biomed. Opt.* **2014**, *19*, 036021.

[29] S. Tzoumas, A. Zaremba, U. Klemm, A. Nunes, K. Schaefer, V. Ntziachristos, *Opt. Lett.* **2014**, *39*, 3523.

[30] a) A. Rosenthal, D. Razansky, V. Ntziachristos, *IEEE Trans. Med. Imaging* **2010**, *29*, 1275; b) S. Tzoumas, N. C. Deliolanis, S. Morscher, V. Ntziachristos, *IEEE Trans. Med. Imaging* **2014**, *33*, 48.